

Discrete Ordinates Quadratures Based on Linear and Quadratic Discontinuous Finite Elements over Spherical Quadrilaterals

Cheuk Y. Lau* and Marvin L. Adams

Texas A&M University, Department of Nuclear Engineering, College Station, Texas 77843-3133

Received January 31, 2016

Accepted for Publication July 20, 2016

Abstract — We present a new family of discrete ordinates (S_n) angular quadratures based on discontinuous finite elements (DFEMs) in angle. The angular domain is divided into spherical quadrilaterals (SQs) on the unit sphere surface. Linear discontinuous finite element (LDFE) and quadratic discontinuous finite element (QDFE) basis functions in the direction cosines are defined over each SQ, producing LDFE-SQ and QDFE-SQ angular quadratures, respectively. The new angular quadratures demonstrate more uniform direction and weight distributions than previous DFEM-based angular quadratures, local refinement capability, strictly positive weights, generation to large numbers of directions, and fourth-order accurate high-degree spherical harmonics (SH) integration. Results suggest that particle-conservation errors due to inexact high-degree SH integration rapidly diminish with quadrature refinement and tend to be orders of magnitude smaller than other discretization errors affecting the solution. Results also demonstrate that the performance of the new angular quadratures without local refinement is on par with or better than that of traditional angular quadratures for various radiation transport problems. The performance of the new angular quadratures can be further improved by using local refinement, especially within an adaptive S_n algorithm.

Keywords — Angular quadrature, discrete ordinates, radiation transport.

Note — Some figures may be in color only in the electronic version.

I. INTRODUCTION

We present a new family of discrete ordinates (S_n) angular quadratures based on discontinuous finite elements (DFEMs) in angle for solving the linear Boltzmann transport equation¹ (LBE). The new angular quadratures have many desirable properties. By design, they are well suited for adaptive S_n algorithms: They are locally refinable, have strictly positive weights, and lend themselves to accurate mapping across multiple refinement levels. They also offer advantages over traditional angular quadratures for standard (nonadaptive) S_n calculations, producing in many problems more accurate solutions with fewer unknowns. The new angular quadratures can be generated with large numbers of directions; for example, we have generated sets with ≈ 800000 directions over all octants.

The new angular quadratures without local refinement can integrate smooth functions with fourth-order truncation error. While many of the preceding advantages also apply to previous DFEM-based angular quadratures,^{2,3} the new angular quadratures offer advantages over their predecessors, which are mainly attributed to more uniform direction and weight distributions. A potential downside of DFEM-based angular quadratures is the inexact integration of spherical harmonics (SH) functions with degrees above the underlying DFEM basis function order. We discuss the ramifications of imperfect high-degree SH integration in later sections. In this section, we discuss the S_n method for solving the LBE and highlight desirable S_n angular quadrature properties. We then compare traditional [e.g., level symmetric (LS), Gauss-Chebyshev (GC) (Refs. 1 and 4)] and DFEM-based angular quadratures.

The LBE is used to model neutral-particle transport in many physical systems:

*E-mail: cheuk.lau@tamu.edu

$$\begin{aligned} \frac{1}{v(E)} \frac{\partial \Psi(\vec{r}, \vec{\Omega}, E, t)}{\partial t} + \vec{\Omega} \cdot \vec{\nabla} \Psi(\vec{r}, \vec{\Omega}, E, t) \\ + \sigma_t(\vec{r}, E, t) \Psi(\vec{r}, \vec{\Omega}, E, t) = \\ \int_{4\pi} d\Omega' \int_0^\infty dE' \sigma_s(\vec{r}, \vec{\Omega}' \cdot \vec{\Omega}, E' \rightarrow E, t) \Psi(\vec{r}, \vec{\Omega}', E', t) \\ + q(\vec{r}, \vec{\Omega}, E, t). \end{aligned} \quad (1)$$

In practice, each independent variable is discretized to form a large set of algebraic equations that can be iteratively solved. Time discretization with any degree of implicitness results in a series of steady-state problems.¹ We note that the solution of eigenvalue problems also requires a series of steady-state problems. Energy discretization results in a series of one-group equations coupled by the group-to-group scattering term.¹ Applying time and energy discretization to Eq. (1) produces

$$\vec{\Omega} \cdot \vec{\nabla} \Psi(\vec{r}, \vec{\Omega}) + \sigma_t(\vec{r}) \Psi(\vec{r}, \vec{\Omega}) = q_s(\vec{r}, \vec{\Omega}) + q(\vec{r}, \vec{\Omega}), \quad (2)$$

where q is the external source including scattering from other energy groups and q_s is the within-group scattering source defined as

$$q_s(\vec{r}, \vec{\Omega}) = \int_{4\pi} d\Omega' \sigma_s(\vec{r}, \vec{\Omega}' \cdot \vec{\Omega}) \Psi(\vec{r}, \vec{\Omega}'). \quad (3)$$

If we expand Ψ in Eq. (3) in terms of SH functions and σ_s in terms of Legendre polynomials, we obtain

$$q_s(\vec{r}, \vec{\Omega}) = \sum_{l=0}^L \frac{2l+1}{4\pi} \sigma_{sl}(\vec{r}) \sum_{\tilde{m}=-l}^l \phi_{l\tilde{m}}(\vec{r}) Y_{l\tilde{m}}(\vec{\Omega}), \quad (4)$$

where

L = scattering order

σ_{sl} = l 'th Legendre expansion coefficient of σ_s

$Y_{l\tilde{m}}$ = SH function of degree l and order \tilde{m}

$\phi_{l\tilde{m}}(\vec{r})$ = angular flux moment of degree l and order \tilde{m} defined as

$$\phi_{l\tilde{m}}(\vec{r}) = \int_{4\pi} d\Omega \Psi(\vec{r}, \vec{\Omega}) Y_{l\tilde{m}}^*(\vec{\Omega}). \quad (5)$$

We note that SH functions are polynomials of the direction cosines defined as

$$\mu = \cos \gamma \sin \theta, \quad (6)$$

$$\eta = \sin \gamma \sin \theta, \quad (7)$$

and

$$\xi = \cos \theta, \quad (8)$$

where γ and θ are the azimuthal and polar angles, respectively. We insert Eq. (4) back into Eq. (2) to obtain

$$\begin{aligned} \vec{\Omega} \cdot \vec{\nabla} \Psi(\vec{r}, \vec{\Omega}) + \sigma_t(\vec{r}) \Psi(\vec{r}, \vec{\Omega}) \\ = \sum_{l=0}^L \frac{2l+1}{4\pi} \sigma_{sl}(\vec{r}) \sum_{\tilde{m}=-l}^l \phi_{l\tilde{m}}(\vec{r}) Y_{l\tilde{m}}(\vec{\Omega}) + q(\vec{r}, \vec{\Omega}). \end{aligned} \quad (9)$$

The S_n method solves Eq. (9) as a set of discrete directions $\vec{\Omega}_m$ with associated weights w_m , $m = 1 : M$ and approximates angular integrals using finite sums:

$$\begin{aligned} \vec{\Omega}_m \cdot \vec{\nabla} \Psi_m(\vec{r}) + \sigma_t(\vec{r}) \Psi_m(\vec{r}) \\ = \sum_{l=0}^L \frac{2l+1}{4\pi} \sigma_{sl}(\vec{r}) \sum_{\tilde{m}=-l}^l \phi_{l\tilde{m}}(\vec{r}) Y_{l\tilde{m}}(\vec{\Omega}_m) + q_m(\vec{r}), \\ m = 1 : M, \end{aligned} \quad (10)$$

where

$$\Psi_m = \Psi(\vec{\Omega}_m), \quad (11)$$

$$q_m = q(\vec{\Omega}_m), \quad (12)$$

and

$$\phi_{l\tilde{m}}(\vec{r}) \approx \sum_{m=1}^M w_m \Psi_m(\vec{r}) Y_{l\tilde{m}}^*(\vec{\Omega}_m). \quad (13)$$

The set of discrete directions and weights forms an angular quadrature. Angular quadratures must integrate Eq. (10) over the global angular domain to obtain a statement of particle balance. Particle-conservation errors are introduced by the integration of the within-group scattering source:

$$\begin{aligned} \int_{4\pi} d\Omega q_s(\vec{r}, \vec{\Omega}) \\ = \sum_{m=0}^M w_m \sum_{l=0}^L \frac{2l+1}{4\pi} \sigma_{sl}(\vec{r}) \sum_{\tilde{m}=-l}^l \phi_{l\tilde{m}}(\vec{r}) Y_{l\tilde{m}}(\vec{\Omega}_m). \end{aligned} \quad (14)$$

Analytically, the integral of SH functions above the zeroth degree over all angles should be zero (due to the SH orthogonality property); however, angular quadratures are not guaranteed to exactly integrate these functions to zero. Therefore, Eq. (14) becomes

$$\sum_{l=0}^L \frac{2l+1}{4\pi} \sigma_{sl}(\vec{r}) \sum_{\tilde{m}=-l}^l \phi_{l\tilde{m}}(\vec{r}) \sum_{m=0}^M w_m Y_{l\tilde{m}}(\vec{\Omega}_m) \\ = \sigma_{s0}(\vec{r}) \phi_{00}(\vec{r}) + \epsilon, \quad (15)$$

where ϵ is the contamination term arising from the angular quadrature integration errors for the SH functions above the zeroth degree. A statement of exact particle balance requires $\epsilon = 0$, which can only occur if the angular quadrature can exactly integrate SH functions of up to degree L over the global angular domain. If the angular flux solution is smooth, and thus can be well approximated by a SH expansion of degree K over the global angular domain, then Eq. (13) suggests that the angular quadrature must accurately integrate SH functions of up to degree $L + K$ over the global angular domain to accurately form the angular flux moments. However, in many practical problems of interest, the angular flux solutions are not smooth but rather are peaky, nearly discontinuous, and have significant magnitudes only in small local angular regions. In order to accurately form the angular flux moments for these problems, angular quadratures must accurately integrate piecewise discontinuous functions whose discontinuities can occur anywhere in the angular domain. In addition, uniform quadrature directions and weights are desired because nonuniformity leads to differences in the integration of two functions that are simply rotations or translations of each other. Inaccurate local integration of the angular flux solution may lead to artificial peaks and valleys in the spatial distribution of the angular flux moments, also known as ray effects.¹

I.A. Traditional Angular Quadratures

The directions and weights of traditional angular quadratures (e.g., LS and GC) (Refs. 1 and 4) are typically generated to exactly integrate as high-degree SH functions as possible over the global angular domain. An exception is the quadruple range (QR) angular quadrature family, which is generated to exactly integrate SH functions over each octant.^{5,6} Therefore, traditional angular quadratures can exactly integrate the scattering source [Eq. (14)] and avoid introducing particle-conservation errors, even for problems with highly anisotropic scattering. However, traditional angular quadratures inaccurately form the angular flux moments [Eq. (13)] when the angular flux is not a smooth function over the entire angular domain, which occurs even for simple radiation transport problems. Traditional angular quadratures are also static (i.e., directions and weights are selected before run time and kept constant throughout the solution process) and uniform (i.e., directions and weights cannot be added to local angular regions), which is computationally inefficient for

radiation transport problems that may need additional angular resolution only for local angular regions.

I.B. DFEM-Based Angular Quadratures

DFEM-based angular quadratures partition the global angular domain into a set of nonoverlapping angular regions $\Delta\Omega_i$, $i = 1, \dots, I$. We define DFEM basis functions in the direction cosines $b_{ij}(\vec{\Omega})$, $j = 1 : J$ over each $\Delta\Omega_i$, where J is the number of degrees of freedom. For example, linear discontinuous finite element (LDDE) basis functions have four degrees of freedom and are linear in the direction cosines:

$$b_{ij}(\vec{\Omega}) = c_j + c_{\mu,j}\mu + c_{\eta,j}\eta + c_{\xi,j}\xi, \quad j = 1 : 4. \quad (16)$$

We note that b_{ij} is identically zero outside of $\Delta\Omega_i$. The b_{ij} unknowns [i.e., c coefficients in Eq. (16)] are determined by requiring b_{ij} to be cardinal functions at J selected quadrature directions. For example, using LDDE basis functions requires solving the following linear system to determine the c coefficients for each angular region:

$$\begin{bmatrix} 1 & \mu_1 & \eta_1 & \xi_1 \\ 1 & \mu_2 & \eta_2 & \xi_2 \\ 1 & \mu_3 & \eta_3 & \xi_3 \\ 1 & \mu_4 & \eta_4 & \xi_4 \end{bmatrix} \begin{bmatrix} c_1 & c_2 & c_3 & c_4 \\ c_{\mu,1} & c_{\mu,2} & c_{\mu,3} & c_{\mu,4} \\ c_{\eta,1} & c_{\eta,2} & c_{\eta,3} & c_{\eta,4} \\ c_{\xi,1} & c_{\xi,2} & c_{\xi,3} & c_{\xi,4} \end{bmatrix} = \begin{bmatrix} 1 & 0 & 0 & 0 \\ 0 & 1 & 0 & 0 \\ 0 & 0 & 1 & 0 \\ 0 & 0 & 0 & 1 \end{bmatrix}. \quad (17)$$

We expand the angular flux solution in each $\Delta\Omega_i$ using its DFEM basis functions:

$$\Psi_i(\vec{\Omega}) \approx \psi_i(\vec{\Omega}) \equiv \sum_{j=1}^J \Psi_{ij} b_{ij}(\vec{\Omega}), \quad (18)$$

where Ψ_{ij} are the basis function expansion coefficients. Since b_{ij} are cardinal functions at the selected directions, Ψ_{ij} are equal to the angular flux solution evaluated at the selected directions:

$$\Psi_{ij} = \Psi_i(\vec{\Omega}_{ij}). \quad (19)$$

We apply Eq. (19) to Eq. (18) to obtain

$$\Psi_i(\vec{\Omega}) \approx \sum_{j=1}^J \Psi_i(\vec{\Omega}_{ij}) b_{ij}(\vec{\Omega}). \quad (20)$$

We apply Eq. (20) to the integration of the angular flux solution over each $\Delta\Omega_i$ to obtain

$$\int_{\Delta\Omega_i} d\Omega \Psi_i(\vec{\Omega}) \approx \sum_{j=1}^J \Psi_i(\vec{\Omega}_{ij}) w_{ij}, \quad (21)$$

where

$$w_{ij} = \int_{\Delta\Omega_i} d\Omega b_{ij}(\vec{\Omega}). \quad (22)$$

The set of directions $\vec{\Omega}_{ij}$ and weights w_{ij} , $j = 1 : J$ forms the DFEM-based angular quadrature for $\Delta\Omega_i$.

DFEM-based angular quadratures have two main advantages over traditional angular quadratures. First, DFEM-based angular quadratures are designed to integrate functions over individual local angular regions. Therefore, their accuracy does not depend on the function being smooth across multiple local angular regions. In contrast, traditional angular quadratures are designed to integrate functions that are smooth over at least an entire octant. Therefore, DFEM-based angular quadratures should more accurately integrate nonsmooth functions, such as the near-discontinuous angular flux solutions commonly produced in radiation transport problems of interest. Second, DFEM-based angular quadratures support local refinement (i.e., add directions to specific angular regions) by recursively partitioning only the angular regions requiring additional angular resolution. This increases the computational efficiency of radiation transport problems requiring additional angular resolution only for specific angular regions.

A potential drawback of DFEM-based angular quadratures is the inexact integration of high-degree SH functions over the global angular domain, producing particle-conservation errors when the scattering order is greater than the DFEM basis-function order. Another potential concern is that this same lack of exact integration of high-degree SH functions may cause the DFEM-based angular quadratures to be less accurate than other angular quadratures for problems with relatively smooth solutions. However, as discussed Sec. III, the integration error of high-degree SH functions rapidly decreases as we increase the number of quadrature directions. In fact, it decreases by a factor of 16 for every factor of 4 increase in the number of quadrature directions. Our limited testing demonstrates that the particle-conservation error for a problem with anisotropic scattering is negligibly small compared to the error for a given quantity of interest (QOI). We expect to explore this further in future work.

Jarrell and Adams developed DFEM-based angular quadratures using LDFE basis functions in the direction cosines defined over spherical triangular (ST) tessellations of the unit sphere surface.^{2,3} We term their angular quadratures as LDFE-ST angular quadratures. The LDFE-ST

angular quadratures have hexagonal rings of directions that form with much larger weights near the center of the octant as shown in Fig. 1. This type of nonuniformity increases local integration error by preferentially weighting angular regions with a higher density of directions or larger weights. In this paper, we investigate the use of spherical quadrilateral (SQ) tessellations of the unit sphere surface to produce more uniform direction and weight distributions. The use of SQs over the unit sphere has been successful in other applications, such as discontinuous Galerkin transport for weather modeling.⁷ The research presented here also extends the DFEM-based angular quadrature methodology to quadratic basis functions, thereby paving the way toward higher-order DFEM-based angular quadratures that exactly integrate higher-degree SH functions. This may be important for radiation transport problems with highly anisotropic scattering.

In this paper, we present the construction of the LDFE-SQ and quadratic discontinuous finite element (QDFE)-SQ angular quadratures, their accuracy in SH function integration, and their performance on various radiation transport problems using both uniform and local refinement. Finally, conclusions will be drawn from the results.

II. ANGULAR QUADRATURE CONSTRUCTION

II.A. Spherical Quadrilateral Tessellation

The construction of the LDFE-SQ and QDFE-SQ angular quadratures begins by inscribing a cube into the unit sphere as shown in Fig. 2a. To maintain rotational symmetry between each octant, the angular quadratures are generated over one octant and then rotated to the rest. Therefore, we only consider the corner of the cube

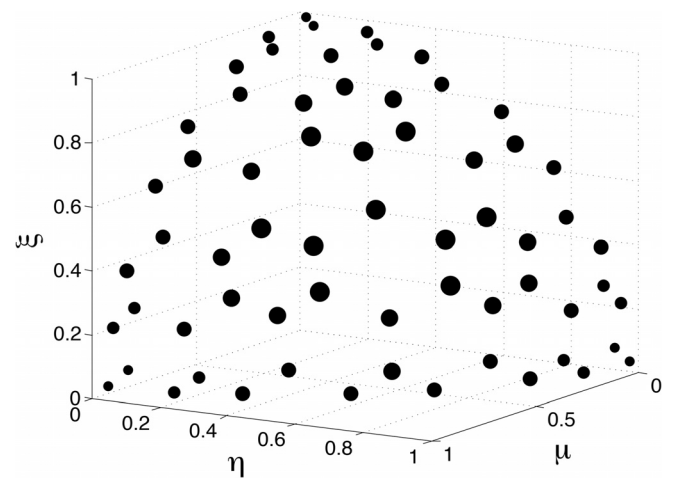


Fig. 1. LDFE-ST angular quadrature for 64 points/octant. Dot sizes are proportional to the weights.

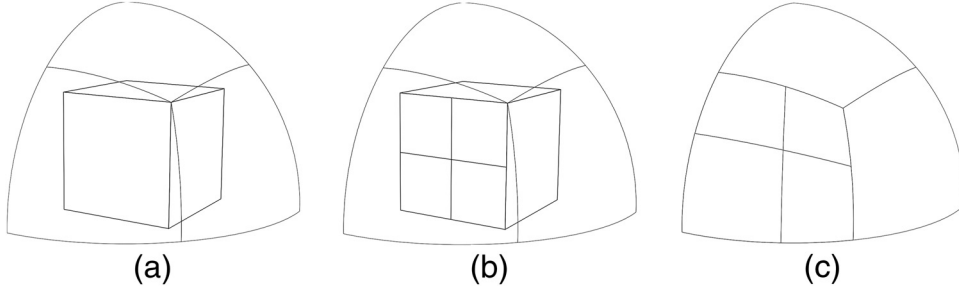


Fig. 2. (a) Corner of the cube inscribed into the first octant of the unit sphere. (b) One of the cube faces divided into sub-squares. (c) Sub-squares projected onto the surface of the unit sphere forming SQs.

belonging to the first octant ($\mu > 0$, $\eta > 0$, and $\xi > 0$). The cube faces in each octant are divided into sub-squares as shown in Fig. 2b and projected onto the surface of the unit sphere to form SQs as shown in Fig. 2c. The cone subtended by each SQ represents a unique partition of the angular domain. To maintain rotational symmetry within each octant, the angular quadratures are generated over one of the cube faces within each octant and then rotated to the rest. Therefore, we consider only the cube face perpendicular to the μ -axis in the first octant. We note that the above symmetry requirements are imposed only for uniformly refined angular quadratures. Locally refined angular quadratures may select specific SQs to further partition.

II.B. DFEM Basis Functions in Angle

We define DFEM basis functions in the direction cosines $b_{ij}(\vec{\Omega})$, $j = 1 : J$ over each SQ i , where J is the number of degrees of freedom. For LDFE-SQ angular quadratures, we use LDFE basis functions in the direction cosines, which have four degrees of freedom and are linear in the direction cosines:

$$b_{ij}(\vec{\Omega}) = c_j + c_{\mu,j}\mu + c_{\eta,j}\eta + c_{\xi,j}\xi, \quad j = 1, \dots, 4. \quad (23)$$

We note that b_{ij} is identically zero outside of SQ i . The b_{ij} unknowns [i.e., c coefficients in Eq. (23)] are determined by requiring b_{ij} to be cardinal functions at four selected quadrature directions. Therefore, we solve the following linear system to find the c coefficients for each SQ:

$$\begin{bmatrix} 1 & \mu_1 & \eta_1 & \xi_1 \\ 1 & \mu_2 & \eta_2 & \xi_2 \\ 1 & \mu_3 & \eta_3 & \xi_3 \\ 1 & \mu_4 & \eta_4 & \xi_4 \end{bmatrix} \begin{bmatrix} c_1 & c_2 & c_3 & c_4 \\ c_{\mu,1} & c_{\mu,2} & c_{\mu,3} & c_{\mu,4} \\ c_{\eta,1} & c_{\eta,2} & c_{\eta,3} & c_{\eta,4} \\ c_{\xi,1} & c_{\xi,2} & c_{\xi,3} & c_{\xi,4} \end{bmatrix} = \begin{bmatrix} 1 & 0 & 0 & 0 \\ 0 & 1 & 0 & 0 \\ 0 & 0 & 1 & 0 \\ 0 & 0 & 0 & 1 \end{bmatrix}. \quad (24)$$

For QDFE-SQ angular quadratures, we use QDFE basis functions in the direction cosines, which have nine degrees of freedom and are quadratic in the direction cosines:

$$\begin{aligned} b_{ij}(\vec{\Omega}) = & c_j + c_{\mu,j}\mu + c_{\eta,j}\eta + c_{\xi,j}\xi + c_{\mu\eta,j}\mu\eta \\ & + c_{\mu\xi,j}\mu\xi + c_{\eta\xi,j}\eta\xi + c_{\xi^2,j}\xi^2 + c_{\mu^2-\eta^2,j}(\mu^2 - \eta^2), \\ & j = 1 : 9. \end{aligned} \quad (25)$$

Again, b_{ij} is identically zero outside of SQ i , and the b_{ij} unknowns [i.e., c coefficients in Eq. (25)] are determined by requiring b_{ij} to be cardinal functions at nine selected quadrature directions. Therefore, we solve the following linear system to find the c coefficients for each SQ:

$$\begin{bmatrix} 1 & \mu_1 & \dots & \mu_1^2 - \eta_1^2 \\ 1 & \mu_2 & \dots & \mu_2^2 - \eta_2^2 \\ \vdots & \vdots & \ddots & \vdots \\ 1 & \mu_9 & \dots & \mu_9^2 - \eta_9^2 \end{bmatrix} \times \begin{bmatrix} c_1 & c_2 & \dots & c_9 \\ c_{\mu,1} & c_{\mu,2} & \dots & c_{\mu,9} \\ \vdots & \vdots & \ddots & \vdots \\ c_{\mu^2-\eta^2,1} & c_{\mu^2-\eta^2,2} & \dots & c_{\mu^2-\eta^2,9} \end{bmatrix} = \begin{bmatrix} 1 & 0 & \dots & 0 \\ 0 & 1 & \ddots & 0 \\ \vdots & \vdots & \ddots & \vdots \\ 0 & 0 & \dots & 1 \end{bmatrix}. \quad (26)$$

II.C. Weight Determination

As discussed in Sec. I.B, the weight of each quadrature direction is the integral of its associated DFEM basis function (i.e., the basis function for which it is cardinal) over its SQ. We define local (\tilde{x}, \tilde{y}) coordinates over the cube face perpendicular to the μ -axis in the first octant as shown in Fig. 3. The LDFE [Eq. (23)] and QDFE [Eq. (25)] basis functions can be

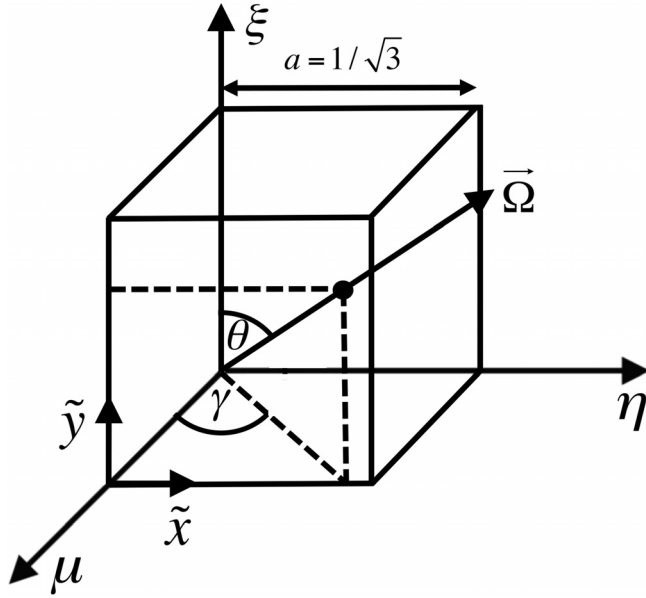


Fig. 3. System of (\tilde{x}, \tilde{y}) coordinates over the cube face perpendicular to the μ -axis in the first octant.

transformed to the (\tilde{x}, \tilde{y}) coordinates by using the following relationships:

$$\mu = \frac{a}{r}, \quad (27)$$

$$\eta = \frac{\tilde{x}}{r}, \quad (28)$$

and

$$\xi = \frac{\tilde{y}}{r}, \quad (29)$$

where $a = 1/\sqrt{3}$ and $r = \sqrt{\tilde{x}^2 + \tilde{y}^2 + a^2}$. The resulting LDFE basis functions are

$$b_{ij}(\tilde{x}, \tilde{y}) = c_j + c_{\mu,j} \frac{a}{r} + c_{\eta,j} \frac{\tilde{x}}{r} + c_{\xi,j} \frac{\tilde{y}}{r}, \quad j = 1 : 4, \quad (30)$$

and the resulting QDFE basis functions are

$$b_{ij}(\tilde{x}, \tilde{y}) = c_j + c_{\mu,j} \frac{a}{r} + c_{\eta,j} \frac{\tilde{x}}{r} + c_{\xi,j} \frac{\tilde{y}}{r} + c_{\mu\eta,j} \frac{a\tilde{x}}{r^2} + c_{\mu\xi,j} \frac{a\tilde{y}}{r^2} + c_{\eta\xi,j} \frac{\tilde{x}\tilde{y}}{r^2} + c_{\xi^2,j} \frac{\tilde{y}^2}{r^2} + c_{\mu^2-\eta^2,j} \frac{a^2 - \tilde{x}^2}{r^2}, \quad j = 1 : 9. \quad (31)$$

The integration of the DFEM basis functions over each SQ i performed over the sub-square SQ i is projected from in the (\tilde{x}, \tilde{y}) coordinates:

$$w_{ij} = \int_{\Delta\tilde{x}_i} d\tilde{x} \int_{\Delta\tilde{y}_i} d\tilde{y} |J| b_{ij}(\tilde{x}, \tilde{y}), \quad (32)$$

where $J = a/r^3$ is the Jacobian mapping from the (\tilde{x}, \tilde{y}) coordinates to the unit sphere surface. One-dimensional Gauss-Legendre quadratures (using 32 points, above which no changes to machine precision are observed) are used to perform the double integral in Eq. (32). The sum of the weights over all octants is normalized to 4π .

II.D. Direction Determination

The placement of the quadrature directions in each SQ fully determines its DFEM basis functions [Eqs. (24) and (26)], which subsequently determine its weights [Eq. (32)]. To determine the placement of the quadrature directions in each SQ, we divide each sub-square into sub-sub-squares as shown in Fig. 4. One quadrature direction starting from the unit sphere origin is required to pass through each sub-sub-square as shown in Fig. 5. To reduce the degrees of freedom in the placement of the quadrature directions, each direction is required to lie on the radius of its sub-sub-square as shown in Fig. 6. We use a multivariate Secant method to iteratively place the quadrature directions such that each resulting weight equals the

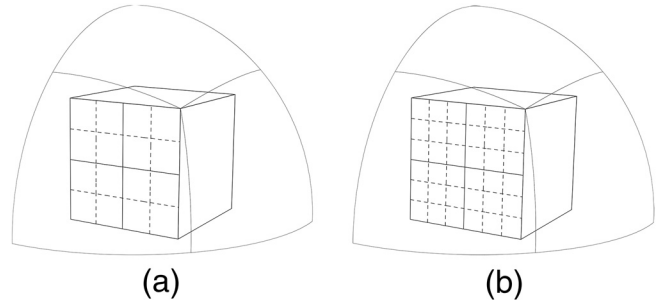


Fig. 4. Sub-sub-square divisions are delineated by dotted lines for (a) LDFE-SQ and (b) QDFE-SQ.

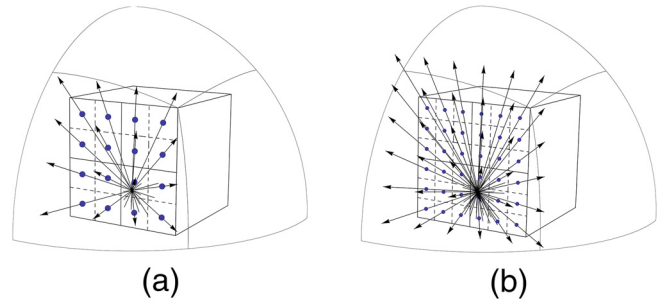


Fig. 5. Quadrature directions are indicated by the arrows for (a) LDFE-SQ and (b) QDFE-SQ. One direction is required to pass through each sub-sub-square delineated by the dotted lines.

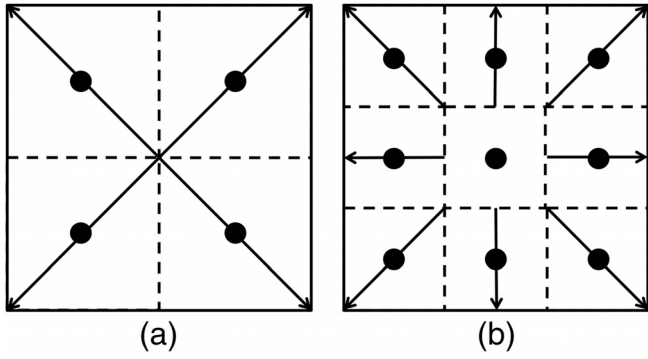


Fig. 6. Sub-sub-square radii delineated by the arrows for (a) LDFE-SQ and (b) QDFE-SQ. One quadrature direction (indicated by the black dots) must pass through each sub-sub-square radius. Note that the quadrature direction is fixed at the center for the center QDFE-SQ sub-sub-square.

surface area of the SQ projected by its sub-sub-square. This results in a geometric angular quadrature, ensuring strictly positive weights and providing a physical significance to the weight distribution. We define the following ratio for each sub-sub-square i :

$$\rho_i = \frac{d}{L}, \quad (33)$$

where d is the distance of the quadrature direction along the sub-sub-square radius and L is the total length of the sub-sub-square radius. The multivariate Secant method begins by making an initial guess for the sub-sub-square ratios $\rho_i^{[0]}$ (e.g., 0.5) and calculating the resulting weights $w_i^{[0]}$. Next, the weights are recalculated by individually perturbing each ratio by a small factor ϵ (e.g., 0.25):

$$\rho_i^{[1]} = \rho_i^{[0]} + \epsilon. \quad (34)$$

The initial $w_i^{[0]}$ and new $w_i^{[1]}$ weights are stored into a weight matrix:

$$W^{[1]} = \begin{bmatrix} w_1^{[0]} & w_2^{[0]} & \cdots & w_J^{[0]} \\ w_1^{[1]} & w_{21}^{[1]} & \cdots & w_{J1}^{[1]} \\ \vdots & \vdots & \ddots & \vdots \\ w_{1J}^{[1]} & w_{2J}^{[1]} & \cdots & w_{JJ}^{[1]} \end{bmatrix}, \quad (35)$$

where w_{ij} is the quadrature weight in sub-sub-square i produced by perturbing the ratio of sub-sub-square j . We consider ratio i to be converged if row i and the first row in the weight matrix are equal. If no ratios are converged, then we solve the following linear system to get the change in ratios δ_i for the next iteration:

$$\begin{bmatrix} \frac{w_{11}^{[1]} - w_1^{[0]}}{\rho_1^{[1]} - \rho_1^{[0]}} & \frac{w_{12}^{[1]} - w_1^{[0]}}{\rho_2^{[1]} - \rho_2^{[0]}} & \cdots & \frac{w_{1J}^{[1]} - w_1^{[0]}}{\rho_J^{[1]} - \rho_J^{[0]}} \\ \frac{w_{21}^{[1]} - w_2^{[0]}}{\rho_1^{[1]} - \rho_1^{[0]}} & \frac{w_{22}^{[1]} - w_2^{[0]}}{\rho_2^{[1]} - \rho_2^{[0]}} & \cdots & \frac{w_{2J}^{[1]} - w_2^{[0]}}{\rho_J^{[1]} - \rho_J^{[0]}} \\ \vdots & \vdots & \ddots & \vdots \\ \frac{w_{J1}^{[1]} - w_J^{[0]}}{\rho_1^{[1]} - \rho_1^{[0]}} & \frac{w_{J2}^{[1]} - w_J^{[0]}}{\rho_2^{[1]} - \rho_2^{[0]}} & \cdots & \frac{w_{JJ}^{[1]} - w_J^{[0]}}{\rho_J^{[1]} - \rho_J^{[0]}} \end{bmatrix} \times \begin{bmatrix} \delta_1 \\ \delta_2 \\ \vdots \\ \delta_J \end{bmatrix} = \begin{bmatrix} SA_1 - w_1^{[0]} \\ SA_2 - w_2^{[0]} \\ \vdots \\ SA_J - w_J^{[0]} \end{bmatrix}, \quad (36)$$

where SA_i is the surface area of the SQ projected by sub-sub-square i . If one or more ratios are converged, we eliminate the corresponding rows and columns from Eq. (36). Last, we calculate the ratios for the next iteration:

$$\rho_i^{[2]} = \rho_i^{[1]} + \delta_i. \quad (37)$$

The multivariate Secant iterations are repeated until $|\delta_i|$ is less than the user-prescribed tolerance for all sub-sub-squares. We note that convergence becomes more difficult with refinement. We found the algorithm described here can converge to $|\delta_i| \leq 10^{-7}$ for up to 161376 and 146016 directions over all octants for the LDFE-SQ and QDFE-SQ angular quadratures, respectively.

II.E. Spherical Quadrilateral Tessellation for Uniform Weights

As discussed in Sec. I.B, a uniform weight distribution is desired to reduce local integration errors. Therefore, we set the sub-sub-square divisions in the (\tilde{x}, \tilde{y}) coordinates such that the surface areas of their projected SQs are as uniform as possible. We group sub-sub-squares for each cube face within an octant into rings starting from the upper-right corner as shown in Fig. 7. The ideal SQ surface area producing a uniform weight distribution is

$$SA_{ideal,sq} = \frac{\pi}{6N_{sq}}, \quad (38)$$

where

N_{sq} = number of sub-sub-squares on the cube face within an octant

$\pi/6 = 4\pi/(8 \times 3)$ = total solid angle associated with the cube face within an octant.

Therefore, the ideal surface area for each ring i is

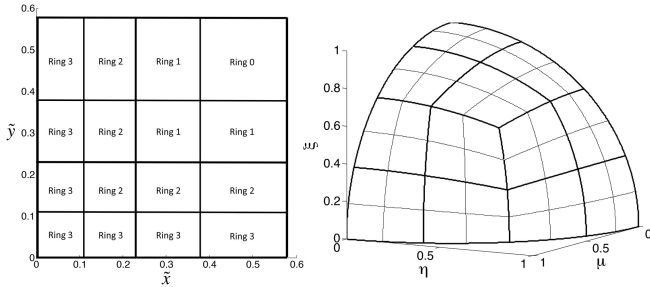


Fig. 7. Sub-square (thick lines) and sub-sub-square (thin lines) divisions are set such that the weight of each ring of sub-sub-squares equals the ideal weight for a uniform sub-sub-square spherical quadrilateral surface area distribution.

$$SA_{ideal,i} = SA_{ideal,sq} N_{sq,i}, \quad (39)$$

where $N_{sq,i}$ is the number of sub-sub-squares in ring i . The sub-sub-square divisions are set such that Eq. (39) is satisfied for each ring. However, Eq. (38) may not be satisfied for each sub-sub-square since the SQ surface areas may differ within a ring. The resulting maximum-to-minimum (respectively, maximum-to-average) weight ratios are no greater than 1.3 (respectively, 1.1) for up to 161376 and 146016 directions over all octants for LDFE-SQ and QDFE-SQ angular quadratures, respectively.

II.F. Refinement Strategy

For uniformly refined LDFE-SQ and QDFE-SQ angular quadratures, we specify a refinement parameter n and divide each of the three cube faces within an octant into $(n+1)^2$ sub-squares. The numbers of directions per octant as a function of n for LDFE-SQ and QDFE-SQ angular quadratures are, respectively,

$$N_{dirs,oct}^{\text{LDFE-SQ}} = 12(n+1)^2 \quad (40)$$

and

$$N_{dirs,oct}^{\text{QDFE-SQ}} = 27(n+1)^2. \quad (41)$$

For locally refined LDFE-SQ and QDFE-SQ angular quadratures, we select specific sub-squares to refine. The refinement of an LDFE-SQ sub-square divides it into four sub-squares by using the old sub-sub-square divisions as the new sub-square divisions. Similarly, the refinement of a QDFE-SQ sub-square divides it into nine sub-squares.

II.G. Comparison to Previous DFEM-Based Angular Quadratures

As discussed in Sec. I.B, the previous DFEM-based (LDFE-ST) angular quadratures developed by Jarrell¹² and

Jarrell and Adams³ used ST tessellations of the unit sphere surface, which produced nonuniform direction and weight distributions. The LDFE-ST angular quadratures formed hexagonal rings of directions with much larger weights near the center of the octant. Figure 8 shows the 108 points/octant LDFE-SQ and QDFE-SQ angular quadratures, which have much more uniform direction distributions than LDFE-ST. Additionally, as discussed in Sec. II.E, the LDFE-SQ and QDFE-SQ angular quadratures have a maximum-to-minimum weight ratio of no greater than 1.3—significantly lower than 5.1 for LDFE-ST. We note that the LDFE-SQ angular quadratures appear to have a more uniform direction distribution than QDFE-SQ. This is a result of the direction placement strategy discussed in Sec. II.D. While the nonuniformity of the QDFE-SQ direction placement could conceivably reduce accuracy in some problems, we observed no negative impact on the results provided in Sec. III.

III. RESULTS

We demonstrate the ability of the LDFE-SQ and QDFE-SQ angular quadratures to (1) accurately integrate increasing-degree SH functions; (2) accurately form the scalar flux for both simple and complex radiation transport problems, while producing particle-conservation errors that are small compared to other discretization errors for radiation transport problems with anisotropic scattering; (3) decrease local integration errors compared to previous DFEM-based angular quadratures; and (4) increase computational efficiency for certain radiation transport problems by using local refinement. The radiation transport problems were performed using the PDT massively parallel discrete ordinates (S_n) transport code,^{8,9} developed at Texas A&M University using the Standard Template Adaptive Parallel Library (STAPL) library.^{10,11}

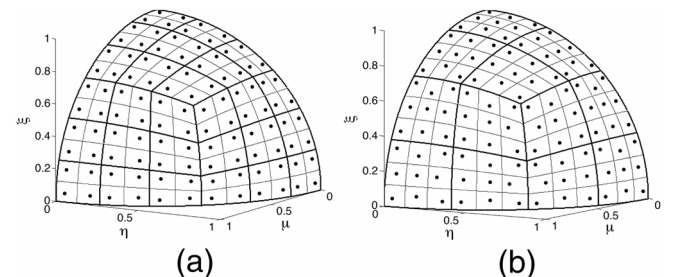


Fig. 8. Angular quadratures of 108 points/octant for (a) LDFE-SQ and (b) QDFE-SQ. Sub-square and sub-sub-square divisions are delineated by the thick and thin lines, respectively. Weights are proportional to the dot area.

III.A. Spherical Harmonic Integration

As discussed in Sec. I, angular quadratures must accurately integrate SH functions of increasing degree in order to avoid particle-conservation errors and to accurately form angular flux moments. The LDFE-SQ and QDFE-SQ angular quadratures were tested to integrate up to 24th-degree SH functions. Because of the octant rotational symmetry of the LDFE-SQ and QDFE-SQ angular quadratures, integrations were only performed over the first octant. The computational results show that LDFE-SQ and QDFE-SQ angular quadratures exactly integrate up to first- and second-degree SH functions, respectively. The LDFE-SQ and QDFE-SQ angular quadratures both integrate all higher-degree SH functions tested with fourth-order accuracy as a function of angular mesh length, defined as $h = 1/\sqrt{\text{number of directions}}$. That is, decreasing h by a factor of n reduces the integration error by n^4 . The reference solutions were obtained analytically. Figures 9, 10, and 11 plot integration error as a function of

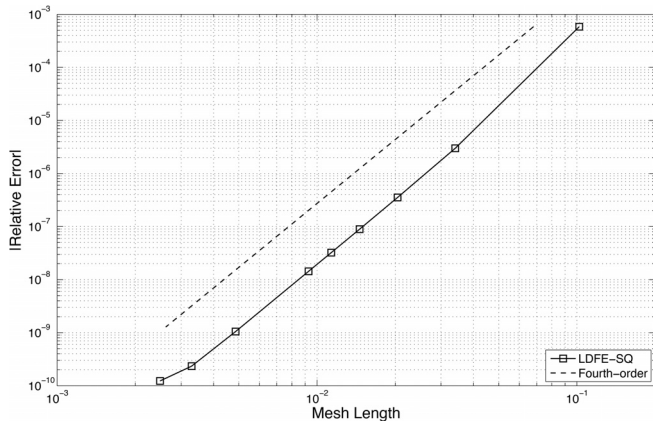


Fig. 9. Integration error for $\mu\eta$ over the first octant using LDFE-SQ angular quadratures. Integration error for $\mu\eta$ using QDFE-SQ is exact to machine precision.

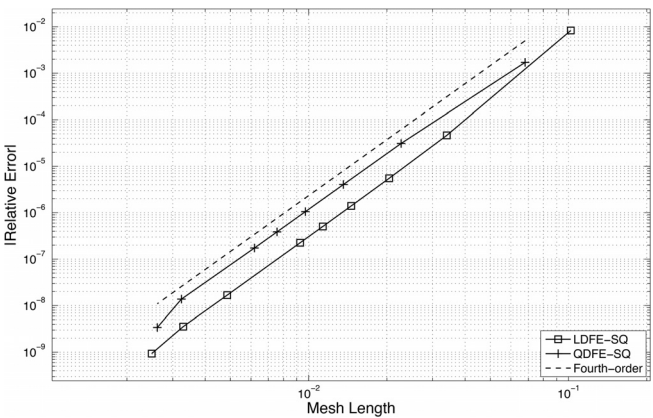


Fig. 10. Integration error for $\mu^3\eta\xi$ over the first octant using LDFE-SQ and QDFE-SQ angular quadratures.

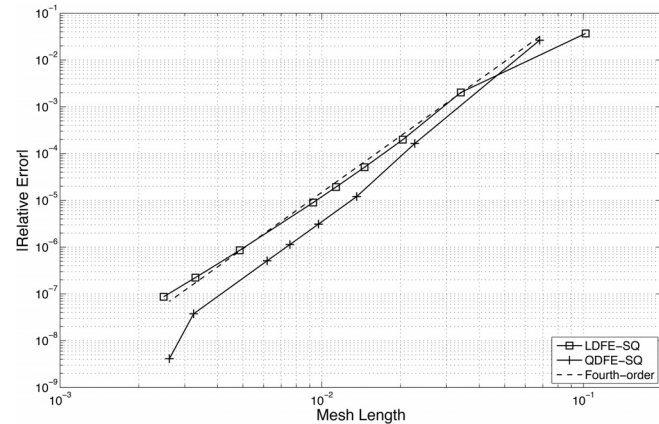


Fig. 11. Integration error for $\mu^3\eta^6\xi^{15}$ over the first octant using LDFE-SQ and QDFE-SQ angular quadratures.

h for selected SH functions ($\mu\eta$, $\mu^3\eta\xi$, and $\mu^3\eta^6\xi^{15}$). We have tested many other polynomials, and all results are similar to those shown. The LDFE-SQ and QDFE-SQ angular quadratures were tested up to 161376 and 146016 directions over all octants, respectively. We note that one might expect the LDFE-based and QDFE-based angular quadratures would exhibit second-order and third-order integration accuracies, respectively. We do not have a theoretical explanation for the observed higher accuracy, which is also seen with the LDFE-ST angular quadratures.

III.B. One-Cell Problem

The one-cell problem demonstrates the ability of the LDFE-SQ and QDFE-SQ angular quadratures to accurately form the scalar flux for a simple radiation transport problem. The one-cell problem is a cube with 1.0-cm sides made of one-group, pure absorber material ($\Sigma_a = 1.0 \text{ cm}^{-1}$) containing a uniformly distributed isotropic source ($q = 1.0 \text{ n/cm}^3 \cdot \text{s} \cdot \text{sr}$) surrounded by vacuum. The piecewise linear discontinuous finite-element method (PWLD) is used for spatial discretization.¹² The one-cell problem was performed using PDT. Figure 12 plots scalar flux error as a function of h . The reference solution was generated using the finest LDFE-ST angular quadrature available containing 524288 directions over all octants. The computational results show that the LDFE-SQ and QDFE-SQ angular quadratures form the scalar flux with fourth-order accuracy as a function of h —significantly better than LS at 1.5-order, triangular GC at second order and on par with the triangular QR and LDFE-ST angular quadratures also at fourth order. The LDFE-SQ and QDFE-SQ angular quadratures were tested up to 161376 and 146016 directions over all octants, respectively.

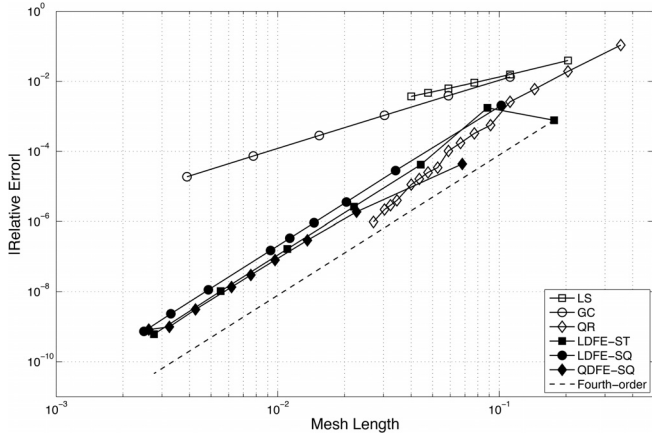


Fig. 12. Scalar flux error for the one-cell problem using LS, triangular GC, triangular QR, LDFE-ST, LDFE-SQ, and QDFE-SQ angular quadratures.

III.C. Spherical Source Problem

The spherical source problem provides a quantitative measure of local integration error for the traditional and DFEM-based angular quadratures. The spherical source problem consists of a spherical source surrounded by vacuum. The spherical source has a radius of 1.0 cm and is made of a pure-absorber material ($\Sigma_a = 1.0 \text{ cm}^{-1}$) containing a uniformly distributed isotropic source ($q = 1.0 \text{ n/cm}^3 \cdot \text{s} \cdot \text{sr}$). The spherical source problem used a ray-tracing method where the scalar flux at a spatial point \vec{r} outside of the spherical source is defined as

$$\phi(\vec{r}) = \frac{q}{\Sigma_a} \sum_{m=1}^M w_m (1 - \exp(-\Sigma_a \ell_m)), \quad (42)$$

where

M = total number of quadrature directions

w_m = weight of quadrature direction m

ℓ_m = chord length for direction m starting from spatial point \vec{r} through the spherical source.

The QOI is the scalar flux at thousands of spatial points distributed across a spherical surface of radius $d = 5.0$ cm concentric with the spherical source. We select the spatial points such that the directions from within the spherical source to each spatial point remain in the first octant. Analytically, the scalar flux should remain constant regardless of position, if d is fixed. However, the computational results show that the calculated scalar flux changes with position due to angular quadrature local integration error. A desirable angular quadrature should minimize the magnitude and

wavelength of these scalar flux oscillations, also known as ray effects.¹ The reference solution was generated using the finest LDFE-ST angular quadrature available containing 524288 directions over all octants.

Figure 13 plots the scalar flux error as a function of spatial position using LS, triangular GC, triangular QR, and LDFE-ST with ≈ 70 directions/octant. The 78 points/octant LS angular quadrature (greatest number of directions with strictly positive weights) produces the most prominent ray effects including the most negative error peaking ($-6.6\text{E-}1$) and the highest root-means-square (rms) error ($2.6\text{E-}1$). The 78 points/octant triangular GC angular quadrature produces much less prominent ray effects than LS as is evident by its lower error peaking ($-2.7\text{E-}1$ to $2.7\text{E-}1$) and rms error ($9.4\text{E-}2$). The 78 points/octant triangular QR angular quadrature also produces less prominent ray effects than LS but has comparable negative error peaking ($-5.9\text{E-}1$). The 64 points/octant LDFE-ST angular quadrature was run using slightly fewer directions since the next available refinement produces 256 directions/octant. The results show LDFE-ST angular quadrature produces three very large error peaks with the highest positive error peaking ($7.1\text{E-}1$). The location of the peaks center around the hexagonal rings of direction that form. Table I summarizes the above results.

Figure 14 plots the scalar flux error as a function of spatial position using triangular GC, triangular QR, LDFE-SQ, and QDFE-SQ with ≈ 105 directions/octant. Overall, the 105 points/octant triangular QR angular quadrature produces the most prominent ray effects including the most negative ($-3.5\text{E-}1$) and positive ($3.1\text{E-}1$) error peaking and the highest rms error ($9.7\text{E-}2$). The 105 points/octant triangular GC angular quadrature produces less prominent ray effects than triangular QR as is evident from its lower error peaking ($-2.4\text{E-}1$ to $2.3\text{E-}1$) and rms error ($7.2\text{E-}2$). The 108 points/octant LDFE-SQ and QDFE-SQ angular quadratures produce lower positive error peaking ($1.8\text{E-}1$ and $1.9\text{E-}1$, respectively) than both triangular GC and triangular QR angular quadratures. The LDFE-SQ and QDFE-SQ angular quadratures produce negative error peaking ($-3.5\text{E-}1$ and $-2.5\text{E-}1$, respectively) that is similar to triangular GC and triangular QR. Table II summarizes the above results.

Figure 15 plots the scalar flux error as a function of spatial position using triangular GC, LDFE-ST, LDFE-SQ, and QDFE-SQ with ≈ 1000 directions/octant. The 1024 points/octant LDFE-ST angular quadrature produces the most prominent ray effects including the most negative ($-5.3\text{E-}2$) and positive ($6.3\text{E-}2$) error peaking and the highest rms error ($1.2\text{E-}2$). This is true despite the fact that the LDFE-ST angular quadrature has a

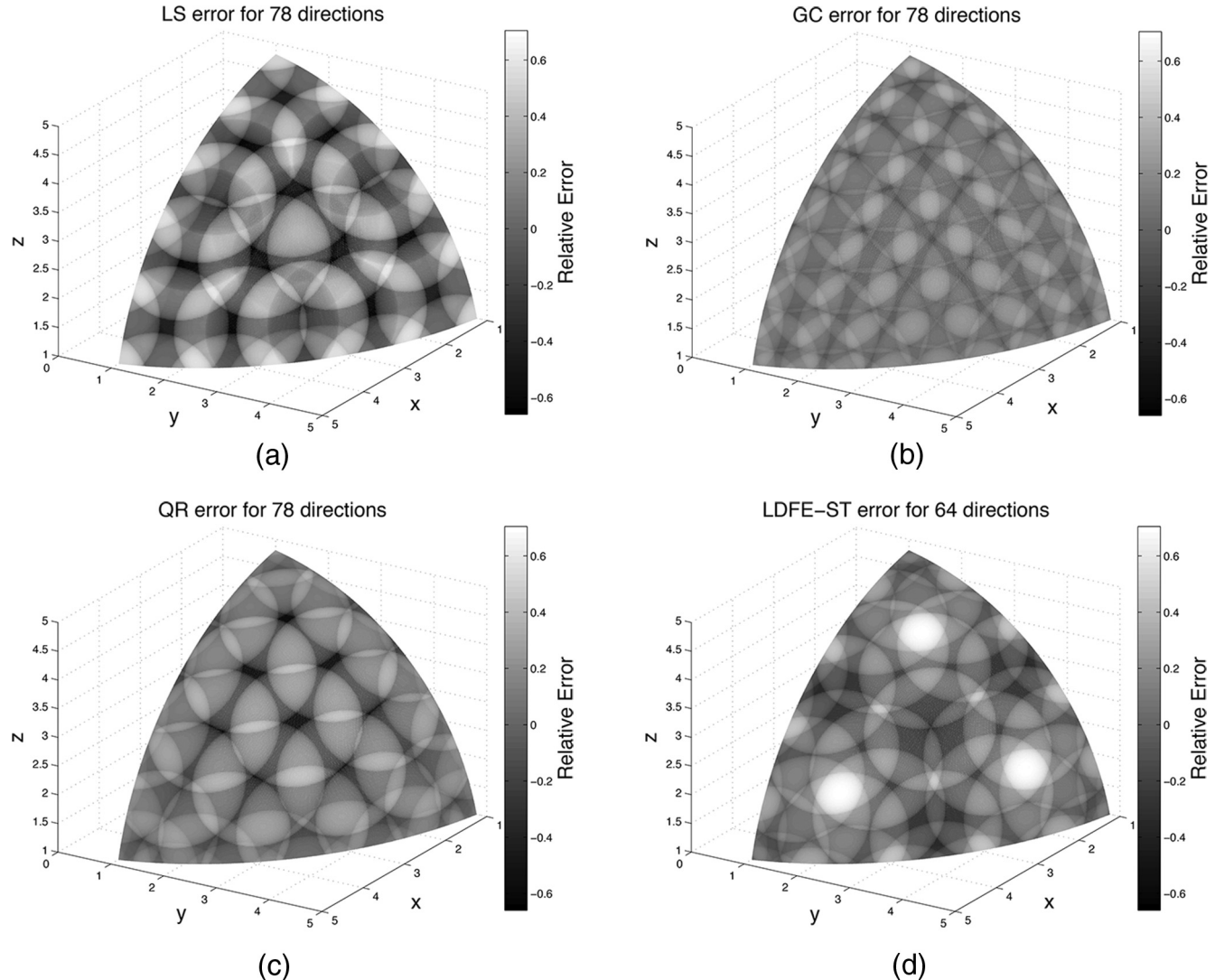


Fig. 13. Scalar flux error as a function of position for the spherical source problem using (a) LS, (b) triangular GC, (c) triangular QR, and (d) LDFE-ST with ≈ 70 directions/octant. Color scales are the same for comparison purposes.

TABLE I

Summary of the Results for the Spherical Source Problem Using LS, Triangular GC, Triangular QR, and LDFE-ST with ≈ 70 Directions/Octant

Parameter	LS	GC	QR	LDFE-ST
Direction count	78	78	78	64
Minimum error	-6.6E-1	-2.7E-1	-5.9E-1	-4.4E-1
Maximum error	5.7E-1	2.7E-1	3.8E-1	7.1E-1
Root-mean-square error	2.6E-1	9.4E-2	1.5E-1	2.0E-1

slightly larger number of directions. The location of the most positive error peaks once again center around the hexagonal rings of directions that form. Table III summarizes the above results.

Figure 16 plots the rms error as a function of angular mesh length. The results show the rms error reduces by second order as a function of h for all angular quadratures except LS.

III.D. Kobayashi Problem

The Kobayashi problem¹³ demonstrates the ability of the LDFE-SQ and QDFE-SQ angular quadratures to accurately form the scalar flux for a complex radiation transport problem. The particular Kobayashi problem considered here is a rectangular block made of pure-absorber material ($\Sigma_{a,1} = 1.0 \text{ cm}^{-1}$) containing a duct ($\Sigma_{a,2} = 10^{-4} \text{ cm}^{-1}$) with sharp, discontinuous bends as shown in Fig. 17. The duct inlet contains a uniformly distributed isotropic source ($q = 1.0 \text{ n/cm}^3 \cdot \text{s} \cdot \text{sr}$ and $\Sigma_{a,3} = 1.0 \text{ cm}^{-1}$). The Kobayashi published reference solution used a ray-tracing method where the scalar flux at a spatial point \vec{r} outside of the source is defined as

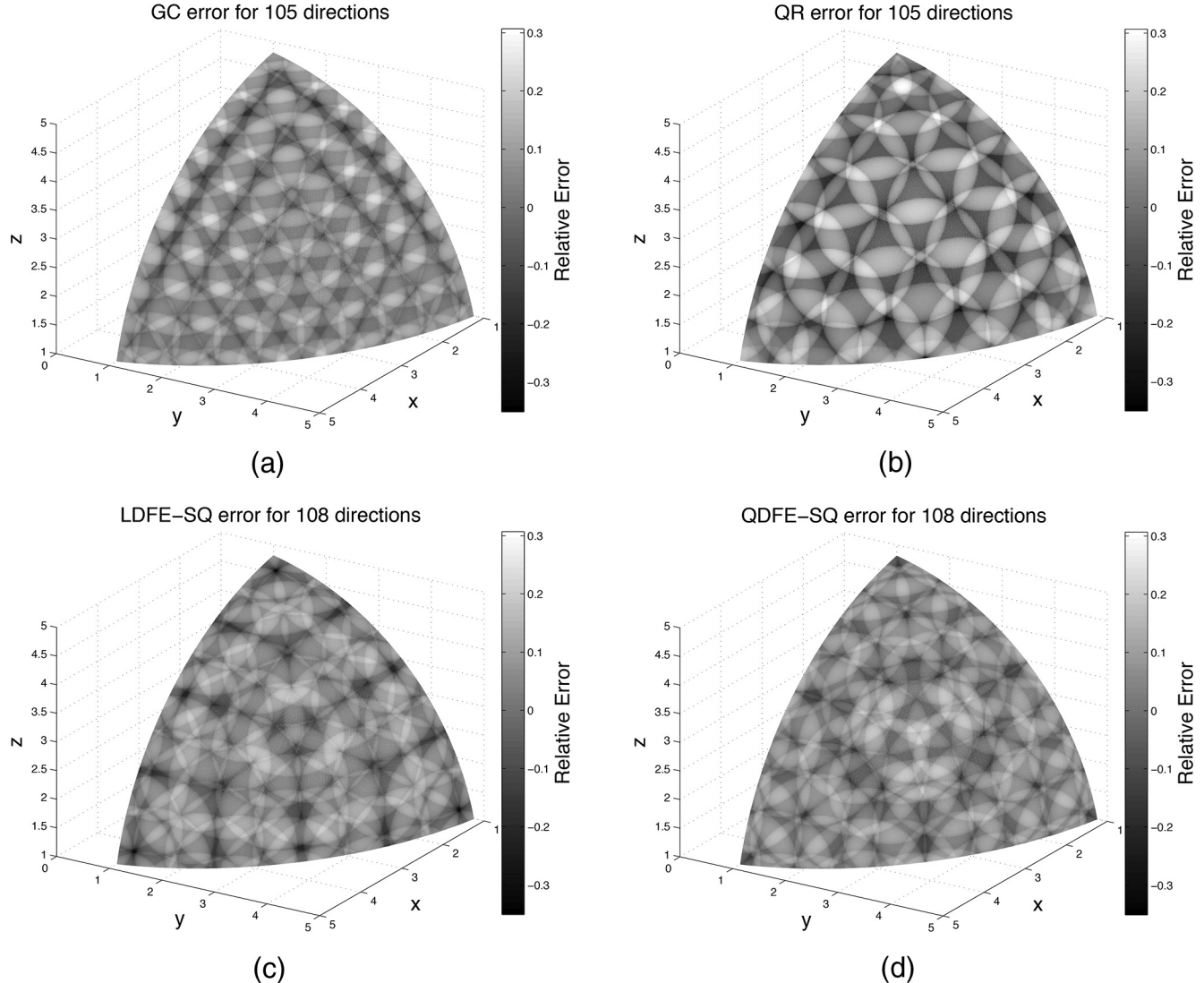


Fig. 14. Scalar flux error as a function of position for the spherical source problem using (a) triangular GC, (b) triangular QR, (c) LDFE-SQ, and (d) QDFE-SQ with ≈ 105 directions/octant. Color scales are the same for comparison purposes.

$$\phi(\vec{r}) = \frac{q}{\sum_{a,3}} \sum_{m=1}^M w_m \exp(-\Sigma_{a,1}\ell_{m,1} - \Sigma_{a,2}\ell_{m,2}) \\ \times (1 - \exp(-\Sigma_{a,3}\ell_{m,3})) , \quad (43)$$

TABLE II

Summary of the Results for the Spherical Source Problem Using Triangular GC, Triangular QR, LDFE-SQ, and QDFE-SQ with ≈ 105 Directions/Octant

Parameter	GC	QR	LDFE-SQ	QDFE-SQ
Direction count	105	105	108	108
Minimum error	-2.4E-1	-3.5E-1	-3.5E-1	-2.5E-1
Maximum error	2.3E-1	3.1E-1	1.8E-1	1.9E-1
Root-mean-square error	7.2E-2	9.7E-2	7.3E-2	6.7E-2

where

M = total number of quadrature directions

w_m = weight of quadrature direction m

$\ell_{m,1}$ = path length along direction m starting from spatial point \vec{r} through the rectangular block made of pure-absorber material

$\ell_{m,2}$ = path length along direction m starting from spatial point \vec{r} through the duct

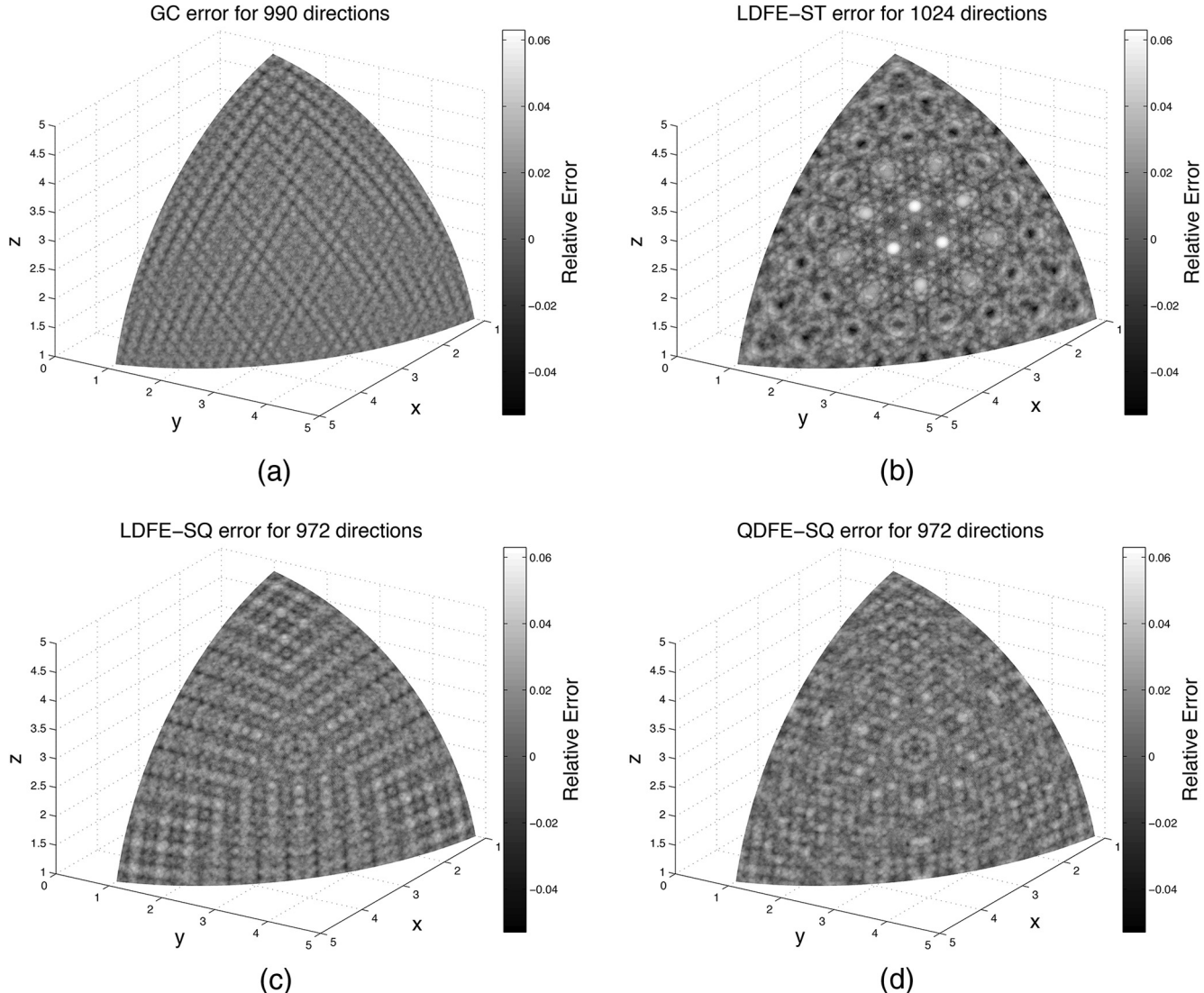


Fig. 15. Scalar flux error as a function of position for the spherical source problem using (a) triangular GC, (b) LDFE-ST, (c) LDFE-SQ, and (d) QDFE-SQ with ≈ 1000 directions/octant. Color scales are the same for comparison purposes.

TABLE III

Summary of the Results for the Spherical Source Problem Using Triangular GC, LDFE-ST, LDFE-SQ, and QDFE-SQ with ≈ 1000 Directions/Octant

Parameter	GC	LDFE-ST	LDFE-SQ	QDFE-SQ
Direction count	990	1024	972	972
Minimum error	-3.6E-2	-5.3E-2	-3.5E-2	-3.7E-2
Maximum error	2.8E-2	6.3E-2	3.8E-2	3.5E-2
Root-mean-square error	8.0E-3	1.2E-2	1.0E-2	9.7E-3

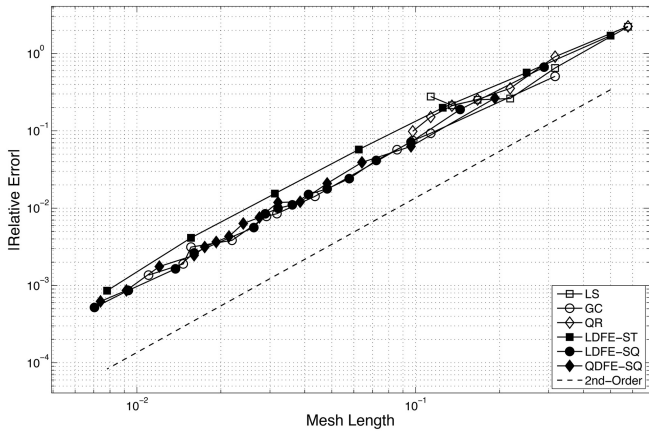


Fig. 16. Root-mean-square error as a function of angular mesh length h for LS, triangular GC, triangular QR, LDFE-ST, LDFE-SQ, and QDFE-SQ angular quadratures.

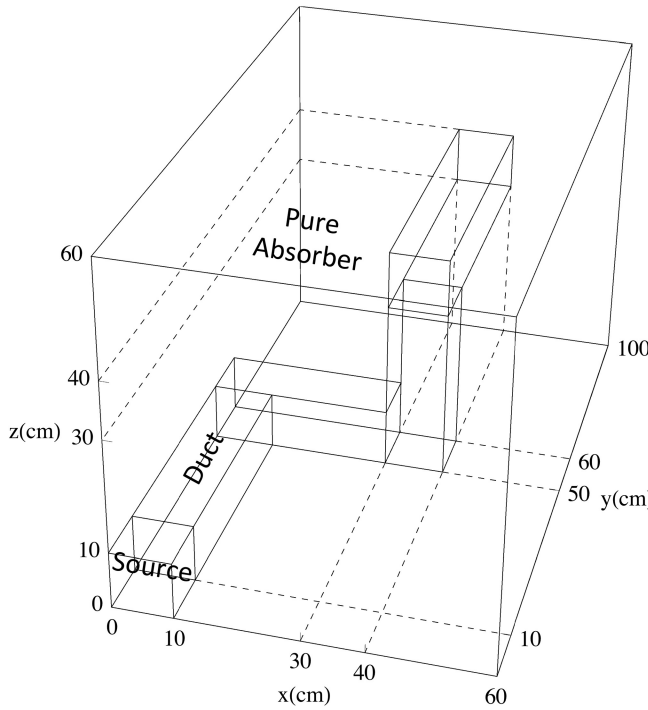


Fig. 17. Setup for the Kobayashi problem with a rectangular block made of pure-absorber material containing a duct with sharp, discontinuous bends and a uniformly distributed isotropic source at the duct inlet.

$$\ell_{m,3} = \text{path length along direction } m \text{ starting from spatial point } \vec{r} \text{ through the source at the duct inlet.}$$

The QOI is the scalar flux near the duct outlet, specifically at (35, 95, and 35 cm). The LDFE-SQ and QDFE-SQ angular quadratures were tested up to 161376 and 146016 directions over all octants, respectively. The published reference solution¹³ was used to calculate the scalar flux errors.

We note that other versions of the Kobayashi problem include scattering. In this research, we chose the pure-absorber version because the addition of scattering tends to smooth the angular variation of the angular flux thereby making it easier for angular quadratures to integrate. Other pure-absorber problems could have been chosen for this study, and we recognize that the duct does not play a large role in the solution when there is no scattering. We chose the Kobayashi problem because it is well known and has a well-vetted published reference solution. We plan to study the Kobayashi problem with scattering in future work.

III.D.1. Uniform Refinement

Figure 18 plots scalar flux error as a function of the angular mesh spacing h , which shows that the order of

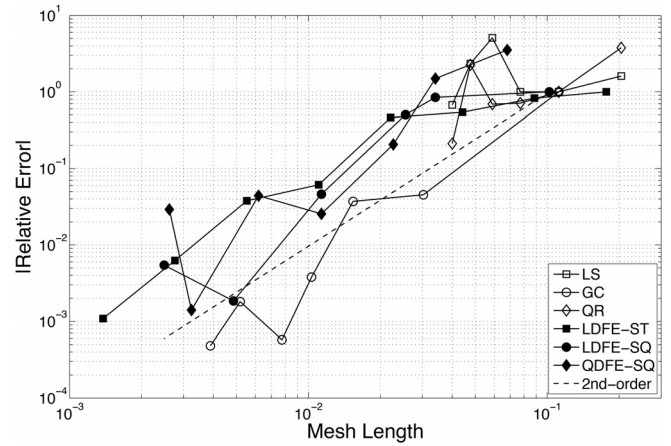


Fig. 18. Scalar flux error at the duct outlet (35, 95, and 35 cm) for the Kobayashi problem using uniform LS, triangular GC, triangular QR, LDFE-ST, LDFE-SQ, and QDFE-SQ angular quadratures.

convergence has decreased for all DFEM angular quadratures compared to the simple one-cell problem from Sec. III.B. The computational results show that the LS angular quadrature produces scalar flux error that oscillates with refinement and remains above 100% until S_{24} (greatest number of directions with strictly positive weights). The remaining angular quadratures (i.e., triangular GC, triangular QR, LDFE-ST, LDFE-SQ, and QDFE-SQ) all produce scalar flux errors that decrease by \approx second order.

III.D.2. Local Refinement

As discussed in Sec. II.F, the LDFE-SQ and QDFE-SQ angular quadratures support local refinement by recursively refining only the angular regions requiring additional resolution. For the Kobayashi benchmark problem, only the angular regions within the cone-of-angle between the source at the duct inlet and the spatial point of interest at the duct outlet (35, 95, and 35 cm) contribute to the QOI. We can reduce memory and run-time requirements without losing accuracy by refining only the angular regions within the cone-of-angle.

Figure 19 plots scalar flux error as a function of h using locally refined LDFE-SQ angular quadrature, which shows that the order of convergence increases from \approx second order using uniform refinement to \approx fourth order using local refinement. The difference in scalar flux error between the uniform and locally refined LDFE-SQ angular quadratures increases with refinement. For example, the uniform LDFE-SQ angular quadrature with $h \approx 2E-2$ produces a relative error of $\approx 2E-1$, whereas the locally refined LDFE-SQ angular quadrature with approximately the same h produces a relative error of $\approx 2E-3$.

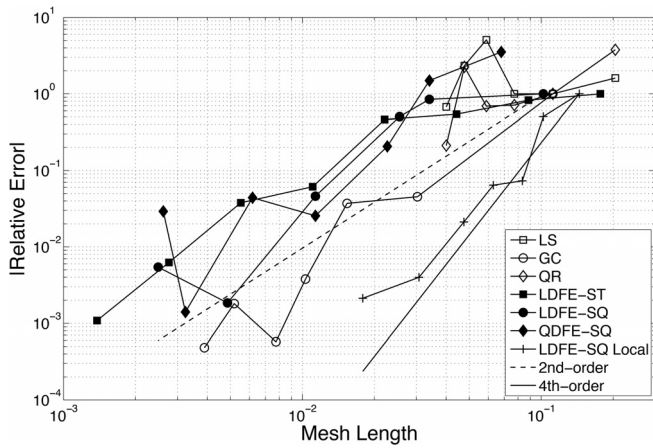


Fig. 19. Scalar flux error at the duct outlet (35, 95, and 35 cm) for the Kobayashi problem using locally refined LDDE-SQ angular quadrature.

III.E. IM-1 Problem

The Impurity-Model-1 (IM-1) problem from the Texas A&M Center for Exascale Radiation Transport demonstrates the ability of the LDDE-SQ and QDFE-SQ angular quadratures to accurately form the scalar flux for a problem with anisotropic scattering, while producing particle-conservation errors that are small compared to other discretization errors affecting the solution. The purpose of the IM-1 experiment is to infer the impurity concentration within a graphite slab, with impurities modeled as an equivalent boron concentration. The IM-1 experiment is illustrated in Fig. 20, consisting of an AmBe source surrounded by high-density polyethylene (HDPE). An air channel connects the AmBe source to a block of graphite. A boron trifluoride (BF3) detector is placed on the other side of the graphite block to measure the exiting neutron flux. The absorption rate in the BF3 detector is used to determine the impurity concentration within the graphite slab. The IM-1 experiment is modeled using fourth-order (P4) scattering. Previous testing indicated that the calculated absorption rate in the BF3 detector does not change significantly using above third-order (P3) scattering. The QOIs for this problem are the absorption rate error in the detector and the maximum particle-conservation error over all spatial cells as a function of h . The absorption rate is

$$R = \sum_{i=1}^{N_e} \sum_{j=1}^{N_s} \Sigma_{a,i} \Phi_{ij} V_j , \quad (44)$$

where

$$N_e = \text{total number of energy groups}$$

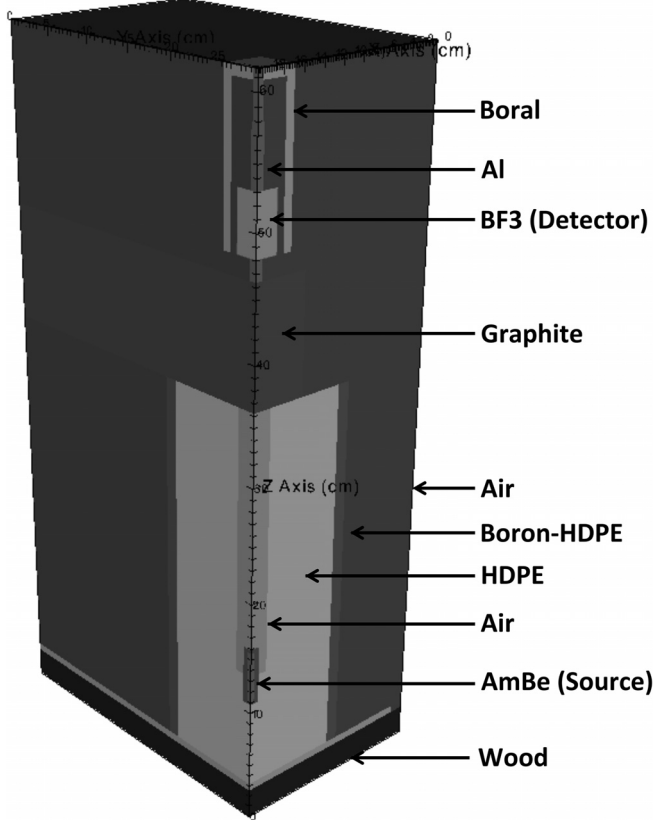


Fig. 20. Setup for the IM-1 problem. Materials as marked.

$$N_s = \text{total number of spatial cells within the detector}$$

$$\Sigma_{a,i} = \text{absorption cross section for energy group } i$$

$$\Phi_{ij} = \text{scalar flux for energy group } i \text{ in spatial cell } j$$

$$V_j = \text{volume of spatial cell } j .$$

The particle-conservation error for each spatial cell is

$$\epsilon = \frac{G - L}{G} , \quad (45)$$

where

$$G = \text{gain rate (from external sources, scattering sources, and inflow)}$$

$$L = \text{loss rate (from absorption and outflow).}$$

The IM-1 problem uses the PWLD method for spatial discretization along with a 99-group structure for energy discretization.

Figure 21 plots the absorption rate error (equivalent to a weighted scalar-flux error, with lower-energy groups having more weight) in the BF3 detector, and the maximum particle-conservation error over all spatial cells as a

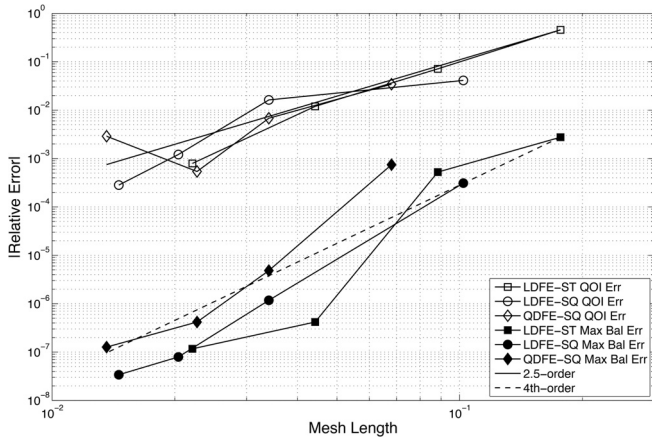


Fig. 21. QOI (absorption rate) error and maximum particle-conservation error as a function of angular mesh length for the IM-1 problem.

function of h . Because of the large computational resources required to run this problem, we did not perform a high-direction angular quadrature run to obtain the reference solution. Instead, the reference solution was found by fitting

$$R_{ref} - R_h = Ch^P, \quad (46)$$

where

R_{ref} = reference absorption rate

R_h = absorption rate for a given h

C = constant

P = error convergence rate.

The results show absorption rate error decreases by ≈ 2.5 order for all DFEM-based angular quadratures, and the maximum particle-conservation error decreases by \approx fourth order as a function of h . We note that the particle-conservation error is several orders of magnitude lower than the absorption rate error for all h .

III.F. Criticality Problem

Next, we demonstrate the ability of the LDFE-SQ and QDFE-SQ angular quadratures to accurately calculate the eigenvalue k_{eff} of a simple criticality problem while producing particle-conservation errors that are small compared to other discretization errors affecting the solution. The criticality problem at hand is a two-dimensional square with 12-cm sides surrounded by vacuum. The square is composed of uranium (^{235}U and ^{238}U composite) and modeled using a 33-group structure for energy discretization with third-order (P3) scattering. The problem was run in PDT using the PWLD method for spatial discretization.

The computational results show that the DFEM angular quadratures (i.e., LDFE-ST, LDFE-SQ, and QDFE-SQ) produce small particle-conservation errors ($\approx 1\text{E-}8$ to $1\text{E-}9$) for this particular problem even at low direction counts. Figure 22 plots the k_{eff} error as a function of h using triangular GC, LDFE-ST, LDFE-SQ, and QDFE-SQ angular quadratures. The reference solution was obtained using an 8256 points/quadrant triangular GC angular quadrature. The LDFE-ST, LDFE-SQ, and QDFE-SQ angular quadratures were tested up to 4096, 3888, and 5292 directions/quadrant, respectively. The computational results show that the DFEM angular quadratures rapidly converge to the reference solution before plateauing at the k_{eff} error tolerance of $1\text{E-}6$. The triangular GC angular quadrature converges to the reference solution by second order.

IV. CONCLUSIONS

We have presented a new family of discrete ordinates (S_n) angular quadratures based on DFEMs in angle. The angular domain is divided into cones subtended by SQs on the surface of the unit sphere. LDFE and QDFE basis functions in the direction cosines are defined over each SQ, producing LDFE-SQ and QDFE-SQ angular quadratures, respectively. The placement of the quadrature directions in each SQ fully determines its basis functions, which are required to be cardinal at the selected directions (i.e., each basis function equals one at its associated quadrature direction and zero at the others). The weight of each quadrature direction is the integral of its associated basis function over its SQ. The new angular quadratures are an extension of the LDFE-ST angular quadratures developed by Jarrell and Adams, which define LDFE basis functions in angle over spherical triangles. The use of SQs, combined with our algorithm for defining SQ boundaries and the location of the

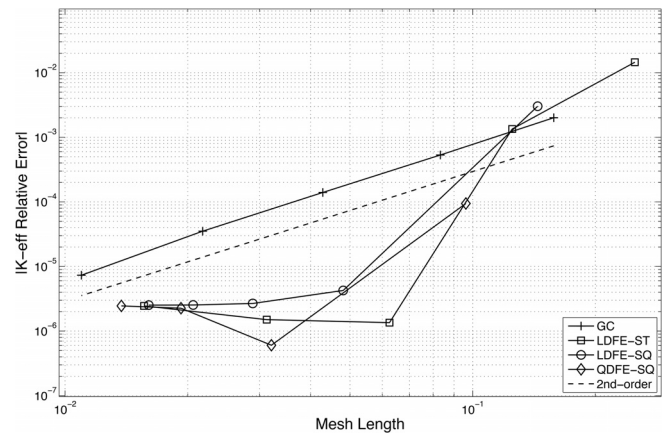


Fig. 22. The k_{eff} error as a function of angular mesh length using triangular GC, LDFE-ST, LDFE-SQ, and QDFE-SQ angular quadratures.

quadrature directions in each SQ, produces more uniform direction and weight distributions, thereby reducing local integration errors. The QDFE-SQ angular quadrature demonstrates the use of higher-order DFEM basis functions within the DFEM-based angular quadrature methodology.

The new angular quadratures are locally refinable, have strictly positive weights that correspond to a geometric tessellation of the unit sphere surface, and can be generated for large numbers of directions (sets with up to ≈ 800000 directions over all octants have been generated). These properties make the new angular quadratures well suited for adaptive S_n algorithms. A potential downside of the new angular quadratures is the inexact integration of SH functions above linear for LDFE-SQ or quadratic for QDFE-SQ, which leads to particle-conservation errors for radiation transport problems with the scattering order above first order for LDFE-SQ or second order for QDFE-SQ. However, the computational results show that the new angular quadratures integrate high-degree SH functions with fourth-order accuracy (i.e., if the average SQ diameter decreases by a factor of 2, then the integration error decreases by a factor of $2^4 = 16$) given uniformly refined quadratures (no local refinement). For this reason, the particle-conservation errors from using the new angular quadratures for a radiation transport problem with anisotropic scattering must rapidly diminish with quadrature refinement, a characteristic observed in our computational results. In the limited testing to date, maximum cellwise conservation errors are orders of magnitude lower than the discretization errors in the QOIs (such as absorption rates or k_{eff}) in the calculations. This result could be different for different QOIs in different problems and may be different if locally refined quadratures are used.

Overall, the computational results indicate that the performance of the new angular quadratures without local refinement is comparable to or better than that of traditional angular quadratures. Their performance can be further improved by using local refinement, which can significantly reduce the number of directions required to achieve a given accuracy, as the computational results presented here have demonstrated for some problems. A major challenge for angular adaptivity is the need for an accurate mapping algorithm for passing the angular flux solution between spatial regions with different angular quadrature refinements. We expect to address this in the future.

Acknowledgments

This work was performed with the support of the National Excellence Fellowship sponsored by Texas A&M University and under the auspices of the U.S. Department of Energy by Lawrence Livermore National Laboratory under contract DE-AC52-07NA27344.

References

1. E. E. LEWIS and W. F. MILLER, *Computational Methods of Neutron Transport*, John Wiley and Sons, New York (1984).
2. J. J. JARRELL, “An Adaptive Angular Discretization Method for Neutral-Particle Transport in Three-Dimensional Geometries,” PhD Dissertation, Texas A&M University (2010).
3. J. J. JARRELL and M. L. ADAMS, “Discrete-Ordinates Quadrature Sets Based on Linear Discontinuous Finite Elements,” *Proc. Int. Conf. Mathematics and Computational Methods Applied to Nuclear Science and Engineering (M&C 2011)*, Rio de Janeiro, Brazil, May 8–12, 2011.
4. A. STROUD and D. SECREST, *Gaussian Quadrature Formulas*, Prentice-Hall, Englewood Cliffs, New Jersey (1966).
5. I. K. ABU-SHUMAYS, “Compatible Product Angular Quadrature for Neutron Transport in x - y Geometry,” *Nucl. Sci. Eng.*, **64**, 299 (1977); <http://dx.doi.org/10.13182/NSE64-299>.
6. I. K. ABU-SHUMAYS, “Angular Quadratures for Improved Transport Calculations,” *Transp. Theory Stat. Phys.*, **30**, 2, 169 (2001); <http://dx.doi.org/10.1081/TT-100105367>.
7. R. D. NAIR, S. J. THOMAS, and R. D. LOFT, “A Discontinuous Galerkin Transport Scheme on the Cubed Sphere,” *Mon. Weather Rev.*, **133**, 814 (2005); <http://dx.doi.org/10.1175/MWR2890.1>.
8. M. P. ADAMS et al., “Provably Optimal Parallel Transport Sweeps on Regular Grids,” *Proc. Int. Conf. Mathematics and Computational Methods Applied to Nuclear Science and Engineering (M&C 2013)*, Sun Valley, Idaho, May 9–15, 2013, American Nuclear Society (2013).
9. W. D. HAWKINS et al., “Efficient Massively Parallel Transport Sweeps,” *Trans. Am. Nucl. Soc.*, **107**, 477 (2012).
10. A. BUSS et al., “STAPL: Standard Template Adaptive Parallel Library,” *Proc. 3rd Annual Haifa Experimental Systems Conf. (SYSTOR 2010)*, Haifa, Israel, May 24–26, 2010.
11. G. TANASE et al., “The STAPL Parallel Container Framework,” *Proc. ACM SIGPLAN Symp. Principles and Practice of Parallel Programming (PPoPP 2011)*, San Antonio, Texas, February 12–16, 2011.
12. H. G. STONE and M. L. ADAMS, “A Piecewise Linear Finite Element Basis with Application to Particle Transport,” *Proc. M&C 2003*, Gatlinburg, Tennessee, April 6–10, 2003, American Nuclear Society (2003).
13. K. KOBAYASHI, N. SUGIMURA, and Y. NAGAYA, “3D Radiation Transport Benchmark Problems and Results for Simple Geometries with Void Regions,” *Prog. Nucl. Energy*, **39**, 2, 119 (2001); [http://dx.doi.org/10.1016/S0149-1970\(01\)00007-5](http://dx.doi.org/10.1016/S0149-1970(01)00007-5).